Impact fragmentation of nanoscale projectiles at ultrahigh striking velocities

S Mastilovic*

Union – Nikola Tesla University, Faculty of Construction Management, Cara Dusana 62-64, 11000 Belgrade, Serbia

Abstract

Molecular-dynamics simulations of the classic Taylor experiment are performed to investigate some general trends of impact fragmentation at ultra-high striking velocities. The striking velocities of flat-ended, monocrystalline, nanoscale pillars (nanoprojectiles) range from 0.34 km/s (Mach 1) to 30 km/s to explore qualitative effects on the fragment mass distribution. These atomistic simulations offer insight into evolution of the fragment distribution and its dependence upon the striking velocity. According to the simulation results, distribution of the fragment masses following hypervelocity impacts of energy sufficient to ensure that the fragmentation problem is statistically well posed, is well represented by the bilinear (bimodal) exponential distribution commonly observed during high-energy homogeneous fragmentation events. At more moderate striking velocities, a mixing of fragments from different fragmentation intensity events—that is, the more pronounced statistical heterogeneity—results in the distribution of fragment masses that appears to follow the trilinear (trimodal) exponential distribution due to the occurrence of a large-fragment tail in addition to the bilinear exponential part. The maximum fragment mass is studied from the standpoint of the striking velocity as well as a set of state parameters: the instantaneous kinetic temperature and the selected stress and strain invariants; corresponding phenomenological relationships are suggested for the investigated hypervelocity impact range.

Keywords

Impact fragmentation · Taylor test · bilinear exponential distribution · hypervelocity impact · extreme loads

1 Introduction

The high-velocity impact of a projectile onto a target triggers a complex sequence of operating deformation and damage mechanisms with different characteristic thresholds and time scales. An integration of these operating mechanisms results in the dynamic response of material characterized by steep deformation gradients and rapid build-up of stress and temperature, which lead to sequential fracture and culminate in energetic expulsion of fragment debris. Importantly, the fragments ejected upon impact contain accumulated damage (i.e., incompletely developed internal cracks or voids) that further evolves during the debris cloud expansion which, depending on availability of the trapped kinetic energy and time, results in the fragmentation process long after the projectile annihilation until the steady-state fragment mass distribution is asymptotically reached. The exploration of development of the debris cloud is of considerable importance in many engineering fields [1]. Intrinsic instabilities in the thermomechanical deformation process at moderate and high strain rates lead to localized deformation with profound effects on the dynamic response of materials on the macroscopic scale. On the other hand, the increase of loading intensity to the ultra-high strain rates results in a transition of the deformation mechanisms from sequential propagation of slips to amorphization [2]. The experimental evidence suggests that fragment mass distributions resulting from dynamic fragmentation of polycrystalline macroscale ductile samples are often exponential or exponential-like (e.g., Gamma, Weibull, Voronoi-Dirichlet [3-5]); notable exceptions are the highly-brittle materials whose dynamic fragmentation differ in

*Corresponding author:
Email: misko3210@yahoo.com , Tel: +381 64 2360-444

fundamental ways from the ductile materials [6]. Molecular dynamics (MD) is a useful tool to investigate the impact fragmentation under ultra-high loading conditions by the high-resolution virtual testing. One of the most advertized advantages of this computational method is the ability to push exploration of physical phenomena beyond current experimental limits.

The ballistic Taylor test [7] is established as a standard procedure to verify dynamic behavior of materials. A series of two-dimensional (2D) traditional MD simulations of this experiment is performed by using flat-ended nanoprojectiles made of the Lennard-Jones 6-12 (L-J) monocrystalline solid, under a tacit assumption that this, admittedly rather simple model is sufficient to capture the salient features of the investigated phenomenon. Due to the overall dimensions of the nanoprojectile (15×110 nm), the nucleation phase of the operating deformation mechanisms and the inelastic flow phase are completed on nanosecond timescale. The set of striking velocities vary within a wide range from 0.34 to 30 km/s with the aim to gain insight into evolution of the fragment mass distribution, the maximum fragment mass dependence upon various state parameters, and explore the impact fragmentation from the standpoint of statistical homogeneity. While the lower end of this range is consistent with existing experimental studies the upper end exceeds them by far in the pursuit of limit features characterizing the ultra-high energy fragmentation (for example, the linear exponential as opposed to the bilinear exponential fragment distribution or the possibility of the terminal fragmentation characterized by the debris cloud consisting entirely of monatomic fragments).

Substantial literature exists in which the fundamental principles of dynamic fragmentation process were investigated both experimentally and theoretically. The lists of crucial references are compiled, among others, in [3-5]; and experimental and theoretical fragment distributions unique to the dynamically loaded brittle solids in [6,8]. The mechanisms, theories and models for dynamic failure and fragmentation are recently summarized in [9,10]. The references cited throughout this paper reflect only the limited objective of the present investigation without any claim to representativeness; a case in point is the brittle fragmentation that is beyond the present scope. Thus, to name but a few milestones, the pioneering work of Lineau [11] on the random geometric fragmentation inspired initially the classical fragmentation studies by Mott [12]. (For the transcripts of the Mott's original wartime reports refer to [4].) Grady and coworkers developed fragmentation theories from both a mechanistic [13,14] and an energetic viewpoints [1,15] focusing principally on the prediction of mean fragment size and some statistical issues of fragment size distribution. Holian and Grady [16] were first to use MD to explore the fragmentation phenomena by simulating a homogeneous 2D adiabatic expansion of condensed matter (aptly termed the microscopic "big bang"). Their results suggested that the cumulative distribution of fragment *masses* was well represented by the bilinear exponential distribution and the average fragment mass could be explained by an energy balance between the kinetic energy of expansion and the potential energy of broken surface bonds. In addition to MD [16-18], examples of computational techniques recently employed in fragmentation investigations include finite element methods [19], meshfree methods [20-22], particle models [23,24], and discrete element models [25].

2 Computer simulation technique

MD is a computer simulation technique frequently used to study evolution of discrete systems at spatial and temporal scales that go beyond the current experimental limits. This investigation is limited to the traditional MD in which the dynamic state of the atomic system is defined by laws of classical mechanics with atomic motions (position vectors $\boldsymbol{r}_i$ and momenta $\boldsymbol{p}_i$) being uniquely determined by empirical potentials. In the present model, a monatomic system (mimicking a monocrystalline, flat-nosed projectile) is comprised of atoms of equal masses $m_i=m_0$ that form an ideal triangular lattice and interact with their nearest neighbors according to the L-J potential [26]. The three L-J model parameters used to match, as close as possible, physical properties of tungsten ($_{74}$W) are the atomic mass $m_0 = 3.1\times10^{-25}$ kg (183.85 u), the atomic radius 1.4 Å ($\equiv r_0/2$ where r_0 is the equilibrium interatomic distance), and the depth of the potential well (the strength of attraction) $\varepsilon_{LJ} = 7.5\times10^{-20}$ J estimated based on the sublimation energy [27]. The Cauchy problem is solved numerically by using the Verlet algorithm [26] with the time step of the

order of femtoseconds estimated in the present simulations based on the fundamental harmonic frequency of the system. The extremely small time step (necessitated by the ultra-high power of the simulated events) in conjunction with an imperative to approach asymptotically a steady-state fragment distribution make these simulations almost prohibitively time-consuming even for the relatively small length scale.

Thus, the distribution of fragment masses is studied during the impact of a slender deformable L-J projectile with a rigid target. The initial temperature of the cluster of atoms, representing the nanoprojectile, is set to zero. (The effect of the initial temperature on the explosive fragmentation of L-J systems was discussed by Diehl et al. [17].) For the continuum scale Taylor impact experiments at moderate striking velocities (in comparison to the velocity range of this MD study), the anvil surface preparation and appropriate lubrication are very important for the damage response of the projectile. The rigid anvil in the current model is represented by a set of immovable atoms that exert a compressive dynamic load on the impacting projectile without any numerical artifices mimicking lubrication, which results in a rough contact surface. Within the present simulation setup, the link between two first-nearest-neighbors atoms ruptures when their interatomic distance exceeds the predetermined critical value $R \approx 1.7\, r_0$. This cut-off interatomic distance is picked to be between the first and second nearest neighbors in the reference configuration. The fragment is defined as a collection (cluster) of atoms with interatomic distance less that the cut-off distance ($r_{ij} \le R$) in a sequential sense (an atom-by-atom search for the nearest neighbors).

The simulations generate information at the nano-scale level: atomic positions and velocities, and interatomic forces. The conversion of this information to macroscopic observables such as stress, strain, and instantaneous kinetic temperature is performed by well-known MD techniques [29-34].

3 Observations and discussion

With reasonable generality it can be asserted that the kinetic energy K_0 of the projectile is during the impact partitioned among the kinetic energy of expulsion of fragment debris and the energy of dissipation absorbed by the projectile through various processes

$$K_0 = K_1 + E_p + E_{th} + E_f \tag{1}$$

In Eq. (1), K_1 is the kinetic energy of the motion of fragments upon the impact, E_p is the energy of plastic dissipation, E_{th} is the energy of deformation-induced heating (shock-induced, for the most striking velocities in this study), and E_f is the fracture energy dissipated through creation of new surfaces in the process of damage accumulation and fragmentation.

Fig. 1. Fragmentation snapshots corresponding to the moment of projectile arrest (a) or full fragmentation (b) for two striking velocities: (a) 0.75 km/s and (b) 3 km/s. Note how the nanoprojectile at striking velocity approaching the hypervelocity impact threshold dissolves in a cloud of particles as the entire projectile is being shattered. This lateral "splash" of the escaping high-temperature debris is similar to the breakup of liquid droplets colliding with a wall as discussed in [28] in connection with the enhanced ductility of fragmenting plastic materials due to the temperature-driven reduction of the shear resistance.

The fragmentation process is statistically well posed if any point of the fragmentation domain is equally likely to fracture. The classic example of such tacit assumption of statistical homogeneity is inherent in the uniform expansion of a ring studied in the Mott's seminal compilation paper [12]. But, in application, the homogeneous fragmentation is rarely achieved. As put succinctly by Grady [4]: "Normally, due to complexity of the device geometry and dynamic loading, the intensity of fracture will vary throughout the body and, correspondingly, the average fragment size will also be a function of position." One objective of the present set of simulations is to study fragment distributions in attempt to capture a (gradual) transition from statistically heterogeneous to homogeneous impact fragmentation. This aim can be achieved by checking to what extent the results of the MD simulations of the homogeneous adiabatic expansion of Holian and Grady [16] remain valid for a highly unidirectional fragmentation process caused by application of a *non-uniform* transient strain-rate field, the basic argument being that given sufficient energy any point of the fragmentation domain is equally likely to fracture even in the latter case.

Thus, the distribution of fragment masses is evaluated periodically during the impact of the slender L-J projectile (15×110 nm, corresponding roughly to the aspect ratio of 7.5) with the rigid target. The nanoprojectile is, in the pristine condition, free of defects; it is believed that this does not affect decisively the hypervelocity-impact MD results presented herein since during the dynamic loading associated with these high and ultra-high strain rates, the evolution of material-texture flaws is, more or less, inhibited by inertial effects (e.g, [35,36]). The simulation results, in terms of the frequency of the certain fragment sizes within the equally spaced regions in the natural logarithm space, are presented in Table 1.

Table 1. Frequency distribution of fragment size n (in number of atoms constituting a fragment) for six striking velocities with the range of data divided into the class intervals of equal width in the logarithmic space. Note that for the hypersonic striking velocities ($v_i \geq 3$ km/s) the projectiles are completely shattered during impact (Fig. 1b). In the other two cases (0.51 and 0.75 m/s), the largest cluster corresponding to the arrested projectile is not included.

		v_i [km/s]					
		0.51	**0.75**	**3**	**5**	**15**	**30**
$\ln n = 0$	$n = 1$	611	2311	9608	11035	17680	20843
$0 < \ln n \leq 1$	$n = 2$	41	212	1094	1510	1637	747
$1 < \ln n \leq 1.5$	$2 < n \leq 4$	11	73	592	754	398	60
$1.5 < \ln n \leq 2$	$4 < n \leq 7$	0	27	219	293	48	0
$2 < \ln n \leq 2.5$	$7 < n \leq 12$	2	7	112	155	2	0
$2.5 < \ln n \leq 3$	$12 < n \leq 20$	1	5	89	86	0	0
$3 < \ln n \leq 3.5$	$20 < n \leq 33$	0	3	49	32	0	0
$3.5 < \ln n \leq 4$	$33 < n \leq 54$	0	3	24	8	0	0
$4 < \ln n \leq 4.5$	$54 < n \leq 90$	0	1	21	5	0	0
$4.5 < \ln n \leq 5$	$90 < n \leq 148$	1	1	6	0	0	0
$5 < \ln n \leq 5.5$	$148 < n \leq 244$	0	1	4	0	0	0
$5.5 < \ln n \leq 6$	$244 < n \leq 403$	0	1	0	0	0	0
$6 < \ln n \leq 6.5$	$403 < n \leq 665$	0	0	0	0	0	0
$6.5 < \ln n \leq 7$	$665 < n \leq 1096$	0	2	0	0	0	0
$7 < \ln n \leq 7.5$	$1096 < n \leq 1808$	0	3	0	0	0	0
$7.5 < \ln n \leq 8$	$1808 < n \leq 2981$	1	0	0	0	0	0

The detailed investigation reveals features of the fragment distribution for various striking velocities obtained with a single run per each velocity. At striking velocity equal to Mach 1 (0.34 km/s) the fragmentation is limited to just a few monatomic fragments. Thus, the nanoprojectile is practically arrested in a damaged state without any notable fragmentation. At Mach 1.2 (0.408 km/s), the number of monatomic fragments increased to a few dozen in addition to a few biatomic fragments but, altogether, the extent of fragmentation is still rather symbolic. The onset of non-negligible fragmentation is identified with the damage-fragmentation transition [25,28,37] and—within the framework of the present simulations— pinpointed roughly at the neighborhood of Mach 1.5 (0.51 km/s). This subjective, qualitative, and, therefore, rather arbitrary initial estimate of the incipient fragmentation velocity ($v_0 \approx 0.51$ km/s) is confirmed by a transparent damage-fragmentation investigation based on the average fragment mass [25]. This method identifies the threshold value v_0 as the striking velocity that coincides with the maximum of $m_{av} = \hat{m}_{av}(v_i)$. The average fragment mass m_{av} is defined as the sample average of the ratio of the second and first moments of fragment masses $m_{av} = \langle \mathcal{M}_2 / \mathcal{M}_1 \rangle$, where the kth moment of the fragment distribution is defined in a single fragmentation event as $\mathcal{M}_k = \sum m^k - m_{\max}^k$ (the summation is performed over all fragments m and $m_{\max}$ is the maximum fragment mass whose contribution is subtracted from $\mathcal{M}_k$).[1] Thus, the *rigid-anvil* impacts for all striking velocities below this breakup threshold ($v_i < v_0$) lead to more or less severe plastic distortion and damage of the nanoprojectile not accompanied by fragmentation. At the incipient fragmentation velocity, the projectile is no longer capable of completely absorbing its kinetic energy (K_0) by plastic distortion and fragmentation takes place.

Furthermore, for projectiles subjected to the high-velocity impact it is of great importance to identify the threshold velocity, v_{fo}, just sufficient to fully fragment the projectile (Fig. 1b). For the present combination of the rigid target and the L-J monocrystalline $_{74}$W, this fragmentation onset velocity is roughly identified to be between 2 and 3 km/s, which agrees rather well with experimental observations reported in literature (e.g., [38]).

Prior to analysis of the simulation results, it is necessary to explain the fragment distribution representation used throughout this paper. In that regard, it is convenient to refer to the first two columns in Table 1 that define the fragment size (mass) class intervals of equal widths in logarithmic space (the natural logarithm is used throughout this article). The notation used henceforth is: n – number of atoms constituting a fragment (cluster), $m = n \cdot m_0$ – the corresponding fragment mass, N – number of the n-atom fragments of mass m, and $M = N \cdot m = N \cdot (n \cdot m_0)$ – total mass of all n-atom fragments. The semilogarithmic plots of fragment debris statistics (Figs. 2, 3, and 5) are obtained by presenting on:

- abscissa - the *arithmetic* mean fragment mass (in number of atoms) of the particular fragment interval (thus, with reference to the second column of Table 2, x-values of data points are equal to 1, 2, 3.5, 6, 10, etc.); and
- ordinate – the total mass of all fragments belonging to the same fragment interval divided by the number of fragment sizes belonging to the same collection of fragments over which the mass accumulation is performed (see caption of Fig. 2 for illustration).

Thus, the ordinate value divided by the corresponding abscissa value represents the number of fragments, which is inherently less noisy, even for the relatively small sample size, due to the described averaging procedure (Fig. 2b). This approach (rather than resolving to the usual presentation of the cumulative number of fragments greater than or equal to a certain fragment mass) has proved beneficial in this study for the determination of the large fragment distribution tail under the small-sample constraints, which is important for the objective of the present investigation.

The first observation with regard to the character of the fragment distribution is that the bilinear exponential distribution of fragment sizes—observed during the uniform adiabatic expansion—appears to hold for the hypervelocity impacts of sufficiently high input energy K_0. The fragment distribution for the striking velocities below and in the range of the hypersonic impact threshold will be argued throughout

[1] It has been argued by Kunn and Herrmann [37] that the strength of the largest fragment $\langle m_{\max} / m_{tot} \rangle$ can be considered to be the order parameter of the damage-fragmentation transition.

this study to exhibit largely the trilinear-exponential features due to the large fragment tail of the distribution (e.g., Fig. 3b and to a certain extent Fig. 2a).

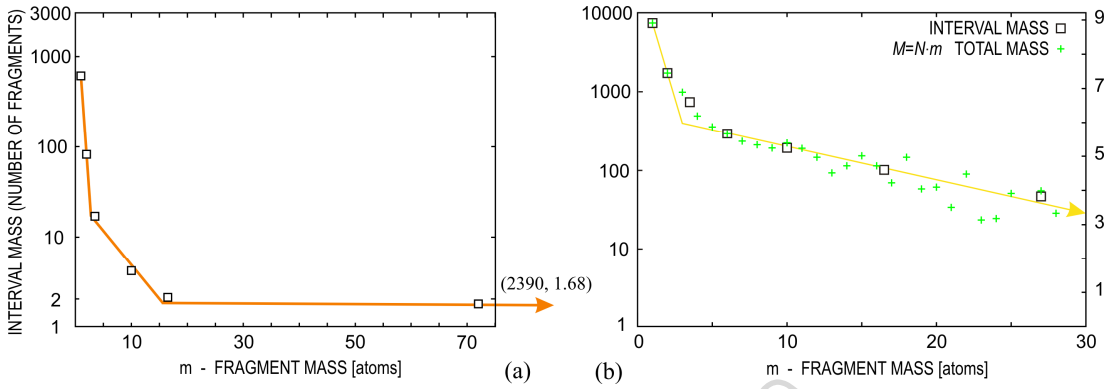

Fig. 2. Semilogarithmic plot of cluster statistics (related to histogram): the number of fragments (N) vs. the fragment mass ($m=n\cdot m_0$) corresponding to: (a) $v_i = v_0 = 0.51$ km/s (the damage-fragmentation transition velocity), and (b) $v_i = 2$ km/s. To clarify further the fragment distribution representation used hereinafter; the first three data points for the former plot are (1, 6.415), (2, 4.407), and (3.5, 2.833); which results from 611 monatomic fragments, 41 biatomic fragments, 10 three-atom fragments, and a single four-atom fragment that yield: $6.415 = ln(611\times1)$, $4.407 = ln(41\times2)$, $2.833 = ln[(10\times3+1\times4)/2]$; note that for the latest data point the cumulative interval mass is divided by number of the fragment classes belonging to that interval. The number of n-atom fragments, $N(m)$, can be obtained as the ratio of the cumulative mass of all n-atom fragments, $M(m)$, and the corresponding fragment mass ($m=n\cdot m_0$). (The mass of the arrested part of the projectile is not considered to be a fragment.)

At the striking velocity of 0.51 km/s (1.5 Mach), corresponding to the incipient fragmentation, the fragment distribution is still rather limited to miniscule fragments: overwhelming majority is monatomic up to four-atom clusters (Table 1). Due to this limited fragmentation and correspondingly small sample size, determination of the fragment distribution is an iffy task but, with respect to Fig. 2a, the fragment mass obeys tentatively the bilinear exponential distribution up to the range of 10-15 atoms. The two isolated large fragments presented in Table 1 define the large fragment tail typical of striking velocities at and below the hypervelocity impact threshold. Occurrence of these large fragments is an outcome of dislocation activities along well-defined and favorably oriented planes, which are operable on (sub)nanosecond timescale due to the nanoscale size of the projectile. (Note that, in general, defect activation, phase transformation, twinning, slip, and dislocation interaction are the operating mechanisms with representative time scales at the nanosecond level.) Fortuitously or not, this large end of the cumulative distribution is close to horizontal (Fig. 2a). The similar trends are observed for $v_i = 0.75$ km/s. It should be emphasized that the fragmentation sample size is relatively small for these, moderate, striking velocities, which may affect the "smoothness" of the corresponding fragment distributions.

The steady-state fragment distributions for a selected set of striking velocities exceeding the fragmentation onset velocity ($v_i > v_{fo}$) are presented in Fig. 3. Fig. 3a is focused on a range of smaller fragments up to the fragment-size interval $(3.5 < \ln n \le 4.0) \leftrightarrow (33 < n \le 54)$. Fig. 3b presents the entire domain of fragment sizes that occur during the Taylor test simulation with the six given striking velocities; the largest interval is $(5.0 < \ln n \le 5.5) \leftrightarrow (148 < n \le 244)$. The simulation results are schematically illustrated with the straight lines representing the least-square fit of data points, to facilitate discussion. Note that these schematics illustrate the probability density functions (histograms) of the respective fragment mass distributions.

Fig. 3a reveals that the small-size fragment population is well represented by the bilinear exponential distribution for *all* hypersonic striking velocities. At sub-hypersonic striking velocities, the fragment distributions, in addition to the bilinear exponential distribution mentioned above, exhibit the large-fragment tail (the "wide shoulder" of the distribution), which results in the trilinear exponential distribution. The fragment mass corresponding to this breakdown of the distribution bilinearity (e.g., approximately 10-15 atoms in Fig. 2a) depends on the striking velocity. This is not surprising bearing in mind that the bilinear exponential distribution is originally obtained within the MD framework [16] under

the uniform conditions of the (statistically homogeneous) adiabatic-expansion simulation that does not favor the occurrence of relatively large fragments.

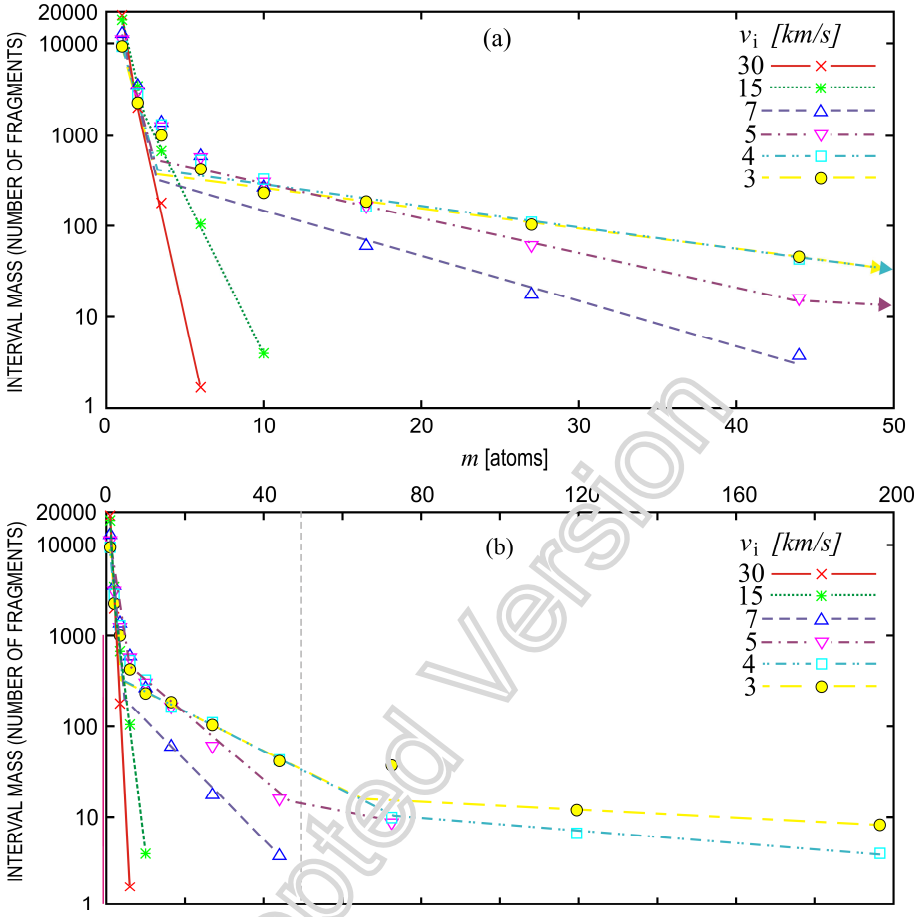

Fig. 3. Semilogarithmic plot of steady-state cluster statistics: the number of fragments (N) vs. the fragment mass ($m=n\cdot m_0$) corresponding to six striking velocities in the hypersonic range. (a) The narrow-shoulder detail, (b) the entire distribution set.

The onset of the bilinear exponential distribution breakdown increases with the impact-velocity increase since more energy becomes available for creation of new surfaces. For $v_i = 0.75$ km/s the fragment mass follows the bilinear exponential distribution up to the range of 25-30 atoms. Simulation results (Fig. 3) for the lower hypersonic range (3-4 km/s) indicate the fragment mass corresponding to bilinear exponential breakdown further increased to approximately 60–70 atoms; for $v_i = 5$ km/s it reduces to 40-50 atoms, while at $v_i \geq 7$ km/s the breakdown seems to disappear, which reflects the increasingly homogeneous fragmentation conditions that finally prevail with further increase of the striking velocity. Obviously, the later condition culminates with the projectile's kinetic energy sufficient to result in the shock-induced adiabatic amorphization, similar to the Holian and Grady's simulations [16]. Actually, based on the critical point data for tungsten estimated by Rachel et al. [39] to correspond to $P_c = (1.1\pm0.2)$ GPa and $T_c = (16000\pm1000)$ K, the present MD simulation results imply that the fragmentation process during the hypervelocity Taylor test ($v_i >$ 3-4 km/s) represents a transition to a homogeneous supercritical fluid since $P > P_c$ and $T > T_c$ [34]. Be it as it may, if the fragment mass, m, is considered a scalar variable, then the random fragmentation is analogous to the 1D Lineau problem [4,11]. The introduction of the rule of Poisson mixtures

$$N(m) = \frac{M(m)}{m} = \sum_{i=1}^{n} N_{0i} \exp\left(-\frac{m}{\mu_i}\right), \quad N_{0i} = \frac{M_{0i}}{m} \tag{2}$$

to capture the salient features of the statistically heterogeneous fragmentation is an inherently reasonable approach to treat the added complexity. The distribution coefficients μ_i are in the present analysis determined as slopes in the semilogarithmic space (e.g., Fig. 3). The Poisson hyper-exponential distribution (2) is a special case of the hyper Weibull distribution proposed by Odintsov ([4] and references therein). (Recall that a number of fragments is considered throughout this paper rather then the cumulative number N_C (>m).) The bilinear exponential form of Eq. (2):

$$N(m) = \frac{M(m)}{m} = N_{01} \exp\left(-\frac{m}{\mu_1}\right) + N_{02} \exp\left(-\frac{m}{\mu_2}\right) \tag{3}$$

emerges in the present investigation at $v_i \approx 5 \div 7$ km/s (Fig. 3). The *cumulative* fragment distribution of the same form was observed by Holian and Grady [16].

With reference to Fig. 3, the increase of the impact energy results in the fragment-distribution transformation defined by the following trend

$$\mu_3 \rightarrow \mu_2 \rightarrow \mu_1 \tag{4}$$

Thus, the trilinear (trimodal) exponential fragment distribution transforms, with v_i increase, into the bilinear (bimodal), which tends to the linear exponential distribution until it, perhaps, reaches the complete annihilation threshold at $v_i = v_1$ (the terminal fragmentation) characterized by the deterministic monatomic fragment distribution ($m_{max} = 1$). Note that, according to [16], the linear exponential distribution is the signature of the homogeneous fragmentation.

In the present study, the narrow-shoulder slope μ_1 of the fragment distribution, is not, like the other two, determined by the least-square fit but is defined by the two data points corresponding to the smallest fragments (that is, the monatomic and biatomic). Thus, this distribution parameter is not defined at the subcritical striking velocities resulting in the negligible monatomic debris (e.g., $v_i \leq 0.34$ km/s) and at $v_i \geq v_1$ (the perhaps-elusive terminal fragmentation characterized by transformation of the entire projectile into the monatomic debris) since the minimum fragment size is 1 atom (Eq. (7$_4$)). In between, the change of μ_1 with striking velocity in semilogarithmic space assumes a characteristic bell shape illustrated in Fig. 4. Based on the simulation results, the saturation value (the upper horizontal asymptote) is roughly μ_1=2/3.

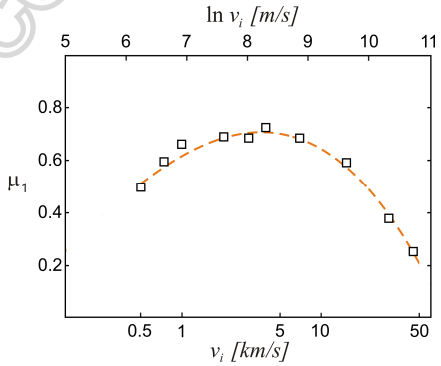

Fig. 4. Change of the slope of the bilinear fragment distribution corresponding to the monatomic peak (μ_1) with the striking velocity. The dashed line corresponds to the third-order polynomial fit of the simulation data.

3.1 Evolution of the fragment mass distribution

Three types of energy dissipation inherent in the fragmentation process, Eq. (1), are captured by the present simulation setup. Notably, the energy expenditure for the new surface creation in the ductile materials accounts for only a small fraction of the input energy. Thus, the kinetic energy K_0 of the

projectile is during the impact partitioned primarily between the kinetic energy of the fragment debris expulsion and the energy of plastic distortion absorbed by the projectile; Eq. (1). An important aspect of fragmentation is that the fragments flying apart contain the internal damage (the incompletely grown internal surfaces) and abundant vibrational energy available for further fragmentation (the trapped kinetic energy of the fragment parts with respect to its center of mass). Consequently, until the steady fragment configuration is approached asymptotically, the damage accumulation and the resulting fragmentation are continuous events and the fragment size distribution is not a complete measure of the damage to the projectile.

Evolution of the cluster statistics presented in Fig. 5 illustrates the continuous change of the fragment mass distribution in the post-collision phase. A sufficient energy given, the fragmentation process appears to evolve towards the complete (monatomic) annihilation in a cascading manner illustrated in Fig. 5 and Table 2 and described by relation (4). (Note that the fragmentation process resulting in the monatomic and biatomic fragments only, would, by definition, correspond to the linear exponential fragment mass distribution that begins to emerge in Fig. 5.)

The evolution of the "narrow-shoulder" fragment distribution coefficient suggested by the simulation results (Fig. 6) is inversely proportional to time

$$\mu_1 \propto t^{-1} \tag{5}$$

On the other hand, μ_2 values presented in Table 2 assume seemingly well-defined discrete levels, which may suggest that the cascading transition (4) is not continuous. Furthermore, fortuitously or not, μ_2 levels apparently reduce by factor of two while approaching μ_1. This observation requires more careful scrutiny, and perhaps larger-scale simulations, prior to making an attempt to come up with a sensible explanation.

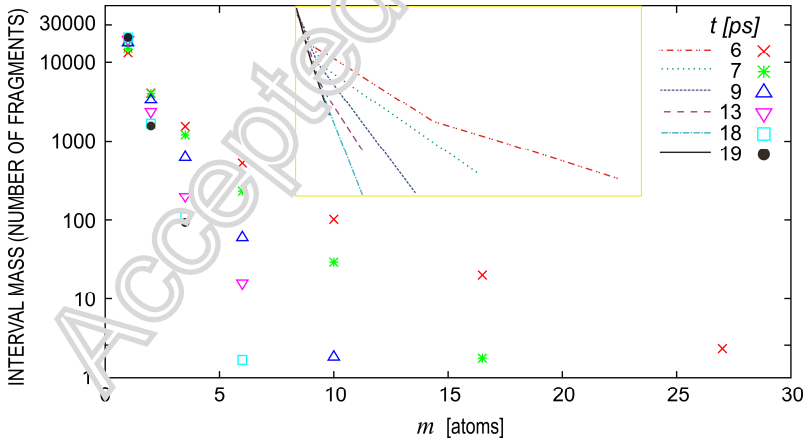

Fig. 5. Evolution of the cluster statistics (main panel) and the corresponding schematic representation (inset) at six different time instances for $v_i = 30$ km/s. Note that the number of fragments approaches the exponential distribution as $\mu_2 \rightarrow \mu_1$. Also note that at 6 *ps* the nanoprojectile is completely dissolved in the debris cloud implying that this cluster statistics evolution is a post-collision process; finally, at 19 *ps* the steady-state fragment mass distribution is practically reached after 190,000 time steps.

Table 2. Evolution of μ-coefficients corresponding to the fragment distributions in the course of 30-km/s impact presented in Fig. 5.

t [ps]	μ_1	μ_2	μ_3
6	0.864	2.30	5.10

7	0.756	2.26	N/A
9	0.594	1.14	N/A
13	0.471	1.13	N/A
18	0.388	0.580	N/A
19	0380	0.540	N/A

Finally, by comparing simulation results presented in Figs. 3 and 5, a similarity of the effects of time and the input energy ($v_i \propto \sqrt{K_0}$) on the fragment mass distribution becomes strikingly apparent. Consequently, the fragmentation evolution could be attributed to the process of distribution of fracture energy necessary to create and coalesce internal surfaces. This energy supply is a common denominator of the phenomenology illustrated by Figs. 3 and 5, which is schematically depicted by Fig. 7.

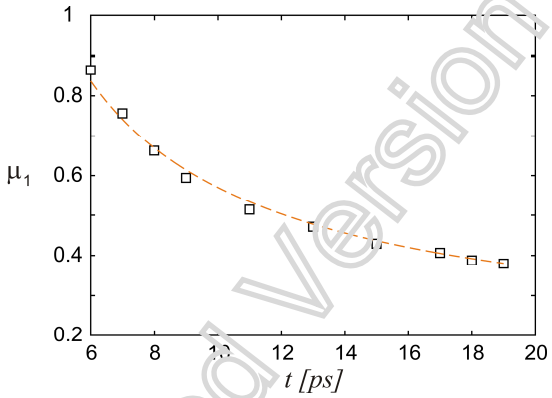

Fig. 6. Time evolution of the narrow-shoulder slope of the bilinear fragment distribution corresponding to the monatomic peak at v_i = 30 km/s. The fitted curve is 0.17+4/t (time in picoseconds).

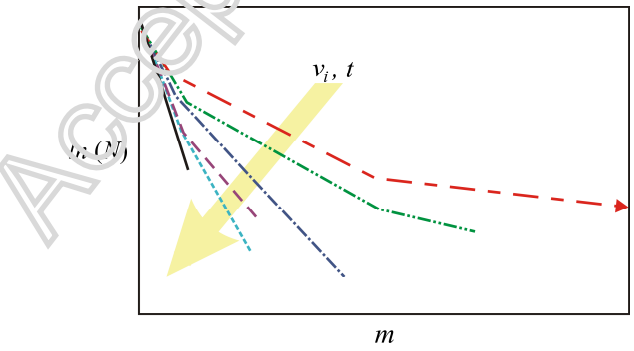

Fig. 7. Schematic representation of the effect of increase of the energy dissipated in a shock-compression process on the fragment distribution. The energy increase indicated by the arrow could be either due to the increase of the striking velocity (Fig. 3) or the increase in duration of the fragmentation process (given sufficient energy) at the fixed striking velocity (Fig. 5).

3.2 Maximum fragment mass

The knowledge of the maximum fragment mass (m_{max}) dependence upon the striking velocity is of obvious interest for engineering applications. While the mean fragment mass illustrates the average character of the dynamic event, the maximum fragment mass, not frequently encountered in the existing literature,

may be of more interest for definition of the design-governing catastrophic event for the structural survival analysis from the standpoint of the extreme value theory.

Fig. 8 suggests that, as a first approximation, beyond the fragmentation onset velocity ($v_i > v_{fo}$) the maximum fragment mass is inversely proportional to the kinetics energy of the projectile

$$m_{\max} \propto v_i^{-2} \quad \Leftrightarrow \quad m_{\max} \propto K_0^{-1} \tag{6}$$

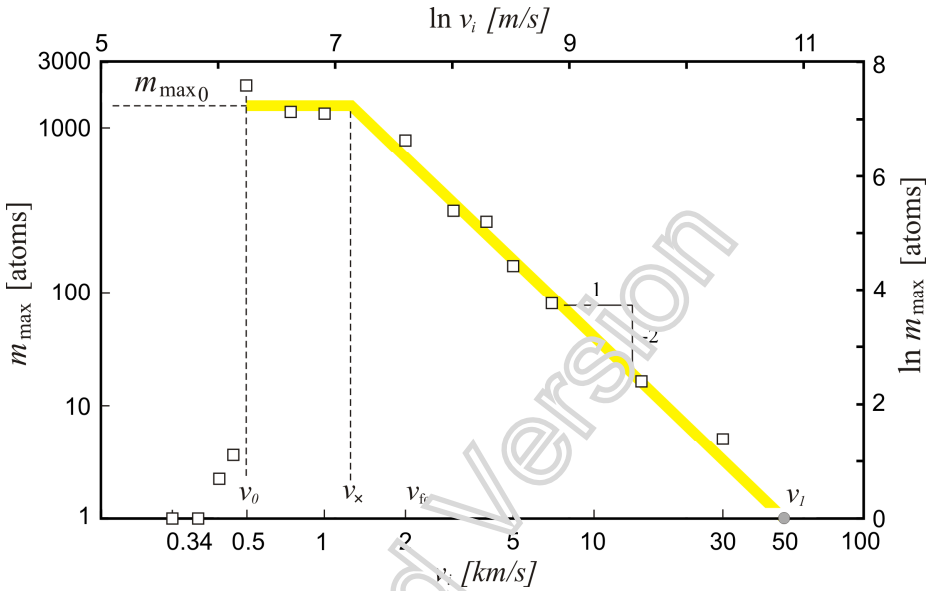

Fig. 8. Logarithmic plot of the maximum fragment mass dependence upon the striking velocity.

With regard to the simulation results presented in Fig. 8, the following expression for the maximum fragment mass can be derived for the linear approximation

$$m_{\max} \begin{cases} << m_{\max 0}, & v_i < v_0 \\ = m_{\max 0}, & v_0 \le v_i \le v_\times \\ = m_{\max 0} \cdot \left(\dfrac{v_i}{v_\times} \right)^{-2}, & v_\times < v_i < v_1 \\ \equiv 1, & v_i \ge v_1 \end{cases} \tag{7}$$

Note that Eq. (7_4) provides only a lower bound of the terminal velocity stemming from the linear approximation, which is yet to be confirmed by actual simulations. By combining Eqs. (7_3) and (7_4), it is straightforward to relate striking velocities corresponding to the terminal fragmentation, v_1, and the crossover, $v_\times$ (Fig. 9):

$$v_1 = v_\times \cdot \sqrt{\frac{m_{\max 0}}{m_{\max 1}}} \tag{8}$$

where $m_{\max 1} \equiv 1$ [atom].

Furthermore, based on Fig. 8, the following empirical formula relates the crossover striking velocity and the fragmentation onset velocity expressed in *km/s*: $v_\times = \sqrt{\Lambda \cdot v_{fo}}$, where the fitting parameter $\Lambda = 1\, km/s$. Therefore, the following empirical estimates follow

$$v_1 = \sqrt{\Lambda \cdot v_{\mathrm{fo}} \cdot \frac{m_{\max 0}}{m_{\max 1}}} \quad \Rightarrow \quad v_1 \approx \sqrt{\Lambda \cdot v_{\mathrm{fo}} \cdot \frac{m_{\max \mathrm{fo}}}{m_{\max 1}}} \tag{9}$$

where the respective units of the striking velocities and the maximum fragment mass are *km/s* and *number of atoms*. The fragmentation onset data used in Eq. (9) are easy to determine experimentally, which enables an estimate of the lower bound of the terminal fragmentation velocity resulting from the linear approximation. Since fragmentation onset data are estimated with reasonable accuracy within the present MD simulation framework ($v_{\mathrm{fo}} \approx 2.5$ km/s and $m_{\max \mathrm{fo}} \approx 800$), the terminal fragmentation lower-bound velocity is determined to be $v_1 \approx 45$ km/s based on Eq. (9_2). It cannot be overstated that, due to the fact that only a miniscule part of K_0 is spent on the fracture process, it is not obvious that *any* impact velocity in the present simulation setup would actually result in the terminal fragmentation ($m_{\max} = 1 \equiv m_{\max 1}$). In any case, the present simulations do not clarify this issue.

3.3 Correlation between the maximum fragment mass and selected state parameters

Three macroscopic observables (2D state parameters) presented henceforth are: the average normal stress, $P = (\sigma_x + \sigma_y)/2$; the instantaneous kinetic temperature, $\mathscr{T}$; and the effective strain, $\varepsilon_{eff} = \sqrt{\left(\varepsilon_x^2 + \varepsilon_y^2\right)/2}$ based on the natural strain definition. The first mechanical stress invariant, P, is a measure of the force interaction between material points inside averaging areas while the instantaneous kinetic temperature, $\mathscr{T}$, is a measure of the intensity of vibratory motion. The evolutions of these three state parameters are recorded at twelve evaluation areas mimicking the measurement gages (eight of them are depicted in Fig. 9). The circular averaging areas designated A-D are spaced equidistantly along the projectile's centerline and have diameter = 12 r_0. The twice-larger averaging areas (diameter = 18 r_0; designated *E-H*) are positioned off the centerline to explore the effects of lateral position and boundary to the state parameters evaluation. The size of evaluation areas are a result of an unavoidable compromise between the contradicting requirements for as large as possible size of the statistical sample and as small as possible resolution length of the analysis.

Be it as it may, it has been verified in the present MD simulations that the stress and temperature results are objective with respect to the evaluation area size; i.e., the larger averaging area results in a somewhat smoother time histories, as expected, but the maximum values are practically the same. Furthermore, the off-centerline averaging areas (*E-H*) record smaller maximum values of the state parameters due to the shorter rise time stemming from the earlier release from the rigid-wall contact.[2]

[2] Importantly, the mechanical stress [32] becomes physically ill-defined as a measure for the mean mechanical force between material points when the averaging area, in the course of projectile distortion and fragmentation, becomes incompletely occupied by atoms (Fig. 9e). It has been verified by the present simulations that the maximum values of the average normal stress ($P_{\max}$) reported henceforth were achieved much before this took place for every single evaluation area. On the other hand, it should be noted that the instantaneous kinetic temperature definition [31,34] is not based intrinsically on the *space averaging* over a certain evaluation area but rather on averaging over *all atoms* covered by the evaluation area; which makes it a state parameter less sensitive to distortion and fragmentation then the mechanical stress.

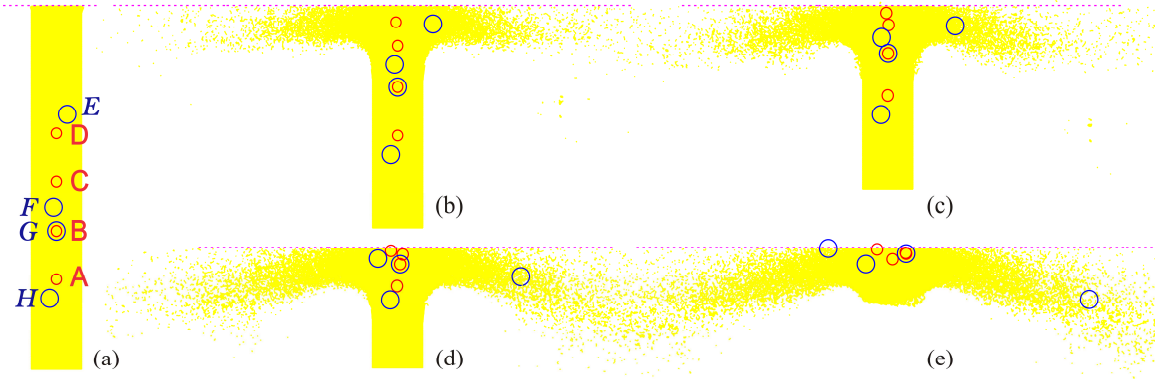

Fig. 9. The sequence of the nanoprojectile deformed configurations at $v_i = 7$ km/s indicating positions of the averaging areas used for the calculation of state parameters: (a) 0.2 ps, (b) 6 ps, (c) 10 ps, (d) 12 ps, (e) 13 ps. Note that the smaller (red) averaging areas designated A-D are located along the centerline while the larger (blue) averaging areas designated *E-H* are slightly off the centerline with exception of *G* that is centered at the same atom as E to explore the effect of the averaging area size.

The logarithmic plots based on the simulation data presented in Fig. 10 indicate that the maximum fragment size is inversely proportional to the maximum values of the pressure and the instantaneous kinetic temperature:

$$m_{\max} \propto P_{\max}^{-1}, \quad m_{\max} \propto T_{\max}^{-1} \tag{10}$$

within the explored part of the hypervelocity impact range. The maximum values of the selected state parameters represent the arithmetic mean of the values evaluated at the points positioned at the centerline of the nanoprojectile. The phenomenological relationships (10) depicted in Fig. 10 reveal indirectly the linearity between pressure and temperature in the ejected plasmatic debris in agreement with the classic ideal gas law.

Although the stress time histories indicate that the stress wave attenuation evidently diminishes with the striking velocity increase, the mechanical stress and instantaneous kinetic temperature fields vary across the fragmentation domain even for the highest impact velocities. Nonetheless, based on the linear fragment mass distributions obtained, it seems that at the higher striking velocities every part of the nanoprojectile is equally likely *to fracture* since even the lowest stress magnitudes achieved are sufficient to brake atomic bonds, which makes the fragmentation process statistically well posed.

Finally, the classic Grady model [15] of dynamic fragmentation due to shear banding in the shock-compressed ductile materials determines the mean spacing of the shear bands to be

$$d = \sqrt{\frac{12\,\mathcal{E}}{\rho\,\dot{\varepsilon}^2}} \tag{11}$$

where $\mathcal{E}$ is the energy dissipated in a steady-wave shock-compression process (approximated by the area between the shock Hugoniot and the Rayleigh line), ρ is the mass density, and $\dot{\varepsilon}$ is the strain rate. When this approach—based on the premise that the interfacial energy created during fragmentation is balanced by the local inertial or kinetic energy of the material—is applied within the present 2D framework, the resulting mean fragment mass is inversely proportional to the square of strain rate. The scaling relation of the same form

$$m_{\max} \propto \dot{\varepsilon}^{-2} \tag{12}$$

is obtained with a reasonable confidence for the maximum fragment mass for the entire hypervelocity impact range based on the simulation results presented in Fig. 11.

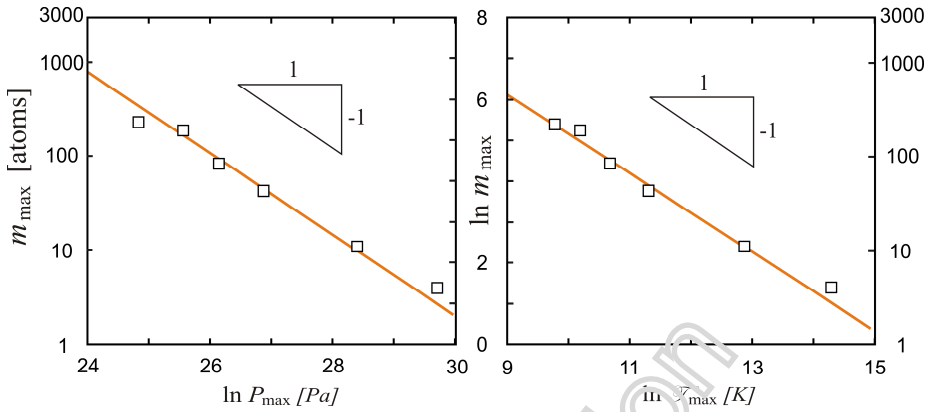

Fig. 10. Logarithmic plot of the maximum fragment mass vs. the maximum values of the pressure and the instantaneous kinetic temperature in the hypervelocity impact range (the data point at the extreme left corresponds to $v_i = 3$ km/s > v_{fo}).

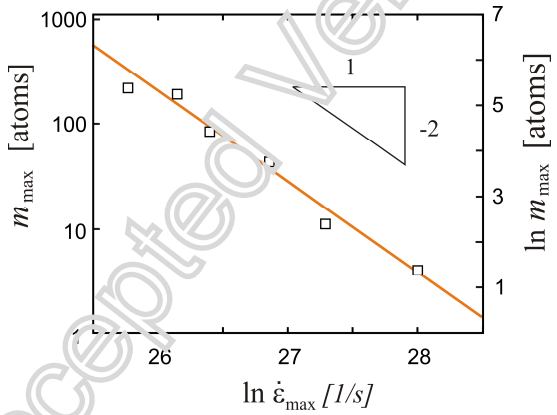

Fig. 11. Logarithmic plot of the maximum fragment mass vs. the maximum strain rate in the hypervelocity impact range (the data point at the extreme left corresponds to $v_i = 3$ km/s, which is slightly above the hypervelocity impact threshold).

4 Conclusions

The current study presents MD simulation of high to ultra-high energy impact loading of a monocrystalline nano-pillar onto a rigid surface (the Taylor test) with aim to explore some qualitative aspects of the fragment mass distribution. The ubiquitous bilinear exponential distribution of fragment mass is apparently innate in a fragmentation process of ductile materials not only for the homogeneous adiabatic expansion but also for the heterogeneous fragmentation phenomena as long as the corresponding sample data set is of a statistically meaningful size. It is, in any case, inherent to the hypervelocity impacts characterized by sufficiently high energy levels. The reduction of striking velocity causes the non-uniform fragmentation that yields, as expected, more complex fragment distributions in accordance to the Poisson's character of the event. According to the present simulation results, the fragment mass distribution, for more moderate striking velocities, is trilinear exponential since, in addition to the bilinear-exponential part, it exhibits a large-fragment tail, illustrated vividly in this article. For the striking velocities below the hypervelocity threshold, perhaps as a consequence of a relatively small

sample size used in the present study, the trilinear character is implied but not as clearly as in the previous case. Nonetheless, the bilinear exponential distribution emerges beyond a doubt in the smaller-clusters region for *every* striking velocity. Details of the cumulative fragment distribution, including the onset of the bilinear exponential distribution breakdown, are naturally highly dependent upon the impact energy. The breakdown threshold increases with increase of the striking velocity until it disappears at the hypervelocity level, which first results in the bilinear, and than the linear, exponential distribution of fragments of completely comminuted nano-projectiles. With regard to the fragment mass distribution, a correspondence is observed between effects of the increase of striking velocity and the increase of fragmentation duration.

The effect of striking velocity on the maximum fragment mass is analyzed resulting in linear empirical relations covering the entire velocity range addressed by the study. These results suggest that, for the most part, the rigid-anvil hypervelocity impact is characterized by the maximum fragment mass inversely proportional to the impact energy of the projectile. This linearity extends to the entire hypervelocity range up to the striking velocities for which relativistic effects cannot be disregarded anymore and the classic-physics billiard-ball approximation of atomic interactions, inherent in the present model, becomes increasingly oversimplified.

The peak values of time histories of the kinematic and thermal parameters of state obtained in the simulations (pressures reaching levels of terapascals and instantaneous kinetic temperatures of ~10^6 K) reflect the extreme character of the hypervelocity collisions. The scaling relationships are offered between the maximum fragment mass and the selected macroscopic observables, which suggest the pressure-temperature linearity characteristic of the ideal gas.

Acknowledgment

This research was partially supported by the Ministry of Education, Science and Technological Development of the Republic of Serbia. The author gratefully acknowledges Dr. Sasha Markovic of PCTech, Belgrade for the many inspiring conversations and programming expertise that he offered to this work.

References

1. Grady DE and Winfree NA (2001) Impact fragmentation of high-velocity compact projectiles on thin plates: A physical and statistical characterization of fragment debris. *Int J Impact Engng* 26: 249-262.
2. Liang W and Zhou M (2004) Response of copper nanowires in dynamic tensile deformation, *Proc Instn Mech Engrs, Part C: J Mech Engng Sci* 214(6): 599-606.
3. Meyers MA (1994) *Dynamic Behavior of Materials*. New York: John Wiley & Sons.
4. Grady DE (2006) *Fragmentation of Rings Shells*, Berlin: Springer.
5. Elek P and Jaramaz S (2009) Fragment Mass Distribution of Naturally Fragmenting Warheads. *FME Transactions* 37 (3): 129-135.
6. Grady DE (2008) Fragment size distributions from the dynamic fragmentation of brittle solids. *Int J Impact Engng* 35: 1557–1562.
7. Taylor GE (1948) The use of flat-ended projectiles for determining dynamic yield stress I. Theoretical considerations, *Proc Royal Soc London A* 194 (1038): 289–299.
8. Herrmann HJ, Wittel FK and Kun F (2006) Fragmentation. *Physica A* 371: 59-66.
9. Zhang H and Ravi-Chandar K (2009) Dynamic fragmentation of ductile materials. *J Phys D: Appl Phys* 42: 214010.
10. Ramesh KT, Hogan JD, Kimberley J, and Stickle A (in press) A review of mechanisms and models for dynamic failure, strength, and fragmentation. *Planetary Space Sci, (Available online 16 December 2014.)*
11. Lineau CC (1936) Random Fracture of a Brittle Solid, *J Franklin Inst* 221: 485-494, 674-686, 769-787.
12. Mott NF (1947) Fragmentation of shell cases. *Proc Royal Soc* A189: 300-308.

13. Grady DE and Kipp ME (1980) Local inertial effects in dynamic fragmentation. *Int J Rock Mech Min Sci* 17: 147-155.
14. Grady DE and Kipp ME (1985) Geometric statistics and dynamic fragmentation. *J Appl Phys* 58(3): 1210-1222.
15. Grady DE (1982) Local inertial effects in dynamic fragmentation. *J Appl Phys* 53(1): 322-325.
16. Holian BL and Grady DE (1988) Fragmentation by molecular dynamics: the micro-scopic "big bang". *Phys Rev Lett* 60: 1355-1358.
17. Diehl A, Carmona HA, Araripe LE, Andrade Jr JS, and Farias GA (2000) Scaling behavior in explosive fragmentation. *Phys Rev E* 62 (4): 4742-4746.
18. He A-M, Wang P, and Shao J-L (2015) Molecular dynamics simulations of ejecta size distributions for shock-loaded Cu with a wedged surface groove. *Computat Mater Sci* 98: 271-277.
19. Levy S and Molinari JF (2010) Dynamic fragmentat ion of ceramics, signature of defect s and scaling of fragment sizes. *J Mech Phys Solid*s 58: 12 –26.
20. Wu Y, Wang D, and Wu C-T (2014) Three dimensional fragmentation simulation of concrete structures with a nodally regularized meshfree method. *Theor Appl Fract Mech* 72: 89–99.
21. Li B, Kidane A, Ravichandran G, and Ortiz M (2012) Verification and validation of the Optimal Transportation Meshfree (OTM) simulation of terminal ballistics. *Int J Impact Engng* 42: 25-36.
22. Li B, Pandolfi A, Ravichandran G, and Ortiz M (2015) Material point erosion simulation of dynamic fragmentation of metals. *Mech Mater* 80: 288–297.
23. Baker KL and Warner DH (2012) Simulating dynamic fragmentation processes with particles and elements. *Engng Fract Mech* 84: 96-110.
24. Kumar V and Ghosh A (2015) Non-linear dynamic fragmentation using Cracking Particles Method. *Comput Mater Sci* 98:117–122.
25. Timár G, Kun F, Carmona HA, and Herrmann HJ (2012) Scaling laws for impact fragmentation of spherical solids. *Phys Rev E* 86 (4): 016113.
26. Allen MP and Tildesley DJ (1996) *Computer Simulation of Liquids*, Oxford: Oxford University Press.
27. Weast RC (1976) *Handbook of Chemistry and Physics*. Cleveland: CRC Press.
28. Timár G, Blömer J, Kun F, and Herrmann HJ (2010) Scaling laws for impact fragmentation of spherical solids. *Phys Rev Lett* 104: 095502.
29. Mastilovic S and Krajcinovic D (1999) Statistical models of brittle deformation: Part II: computer simulations. *Int J Plast* 15: 427-456.
30. Hoover WG (1985) Canonical dynamics: Equilibrium phase space distributions. *Phys Rev A* 31: 1695-1697.
31. Holian BL, Voter AF and Ravelo R (1995) Thermostatted molecular dynamics: how to avoid the Tada demon hidden in Nose-Hoover dynamics, *Phys Rev E* 52: 2338-2347.
32. Zhou M (2003) A new look at the atomic level virial stress: on continuum-molecular system equivalence. *Proc Royal Soc London A* 459: 2347-2392.
33. Buehler MJ (2008) *Atomistic Modeling of Materials Failure*, New York: Springer.
34. Mastilovic S (2014) Molecular-dynamics simulations of the nanoscale Taylor test under extreme loading conditions. *Math Mech Solids* DOI: 10.1177/1081286514522146.
35. Mastilovic S (2011a) Some observations regarding stochasticity of dynamic response of 2D disordered brittle lattices. *Int J Damage Mech* 20: 267–277.
36. Mastilovic S (2011b) Further remarks on stochastic damage evolution of brittle solids under dynamic tensile loading. *Int J Damage Mech* 20: 900–921.
37. Kun F and Herrmann HJ (1999) Transition from damage to fragmentation in collision of solids. *Phys Rev E* 59 (3): 2623-2632.
38. Livingstone IHG, Verolme K and Hayhurst CJ (2001) Predicting the fragmentation onset velocity for different metallic projectiles using numerical simulations. *Int J Impact Engng* 26: 453-464.
39. Rakhel AD, Kloss A, Hess H (2002) On the Critical Point of Tungsten. *Int J Thermophys* 23: 1369-1380.